RSC Sustainability

ROYAL SOCIETY OF CHEMISTRY

PAPER

View Article Online
View Journal | View Issue

Check for updates

Cite this: *RSC Sustainability*, 2025, **3**, 995

ZnO/Co_3O_4 supported on carbon nanotubes as anode materials for high-performance lithium-ion batteries†

Songli Qiu, Jiafeng Wu, Liyu Chen * and Yingwei Li *

Received 6th November 2024
Accepted 5th January 2025

DOI: 10.1039/d4su00691g

rsc.li/rscsus

Metallic oxides show great potential in achieving high specific capacity as electrodes for lithium-ion batteries (LIBs). However, their inherent poor conductivity and significant volume expansion often result in inferior rate performance and reduced stability in electrochemical cycles. Here, we report a composite of ZnO and Co_3O_4 wrapped in carbon nanotubes (denoted as ZnO/Co_3O_4@CNTs) with hierarchically porous architecture *via* pyrolysis–oxidation of a Zn/Co-zeolitic imidazolate framework (ZIF) precursor. The dual-transition metal oxides can undergo abundant redox and alloying reactions with enhanced redox kinetics, while the CNT layers facilitate electron transfer and mitigate volume expansion. As a result, ZnO/Co_3O_4@CNTs exhibits high electrochemical performance with excellent lithium storage capability and high electronic and ionic diffusion kinetics, making it a promising anode material for LIBs. It achieves a high reversible capacity of 1156 mA h g^{-1} at a current density of 200 mA g^{-1} after 200 cycles, with an extremely low capacity degradation rate of about 0.54‰ per cycle.

Sustainability spotlight

The development of electrode materials with excellent rate performance and cycling stability for lithium-ion batteries (LIBs) is essential to meet the growing demand for environmentally friendly, safe, and reliable power sources. Transition metal oxides (TMOs) and carbon materials are two important types of electrodes for LIBs; however, neither can simultaneously achieve high lithium storage capacity, high conductivity, and high stability on its own. Here, we demonstrate that integrating TMOs with carbon tubes combines the strengths of both materials and overcomes the limitations of each component. This composite material can be synthesized efficiently through a one-pot method involving reductive and oxidative pyrolysis of MOFs, which is highly efficient and scalable. Our work supports the UN Sustainable Development Goals of affordable and clean energy (SDG 7) and responsible consumption and production (SDG 12).

1. Introduction

With the increasing demand for environmentally friendly, safe, and reliable power sources, particularly for the growing market of electric vehicles, lithium-ion batteries (LIBs) have become increasingly popular due to their high energy density, low weight, and low cost.[1–3] However, the capacity and life of LIBs tend to decline with repeated charge–discharge cycles, affecting their long-term stability. There is an urgent need to develop electrode materials with exceptional rate performance and cycling stability, which can represent a significant advancement in energy storage technology.[4,5]

Transition metal oxides (TMOs) are promising candidates for LIB electrodes due to their high theoretical specific capacities (800–1000 mA h g^{-1}).[6–9] Double TMOs, with abundant redox active sites, can further enhance lithium storage capacity.[10] However, TMOs suffer from significant volume expansion during lithiation and delithiation, leading to continuous capacity degradation.[11] Moreover, their poor conductivity limits electron transfer, reducing overall rate performance.[12–14] Combining double TMOs with conductive carbon materials, such as carbon nanotubes (CNTs) and graphene, can improve conductivity, enhance the migration rate of Li^+, and increase the efficiency of charging and discharging.[15–17] Additionally, conductive carbon frameworks with sufficient surface areas can buffer volume expansion, maintain mechanical integrity during repeated lithiation/delithiation, and improve cycling stability and rate performance.[18]

Metal–organic frameworks, particularly zeolitic imidazolate frameworks (ZIFs), serve as ideal precursors or templates for the synthesis of effective LIB electrode materials through various pyrolysis methods.[19–22] One approach involves oxidative pyrolysis of ZIFs to produce metal oxides, while another approach is high-temperature carbonization of ZIFs under an inert atmosphere to yield carbon-based materials with good conductivity.[23,24] Despite these advancements, metal oxides alone are prone to agglomeration and volume expansion, while carbon-

Guangdong Provincial Key Laboratory of Fuel Cell Technology, School of Chemistry and Chemical Engineering, South China University of Technology, Guangzhou 510640, China. E-mail: liyuchen@scut.edu.cn; liyw@scut.edu.cn

† Electronic supplementary information (ESI) available. See DOI: https://doi.org/10.1039/d4su00691g

Open Access Article. Published on 06 January 2025. Downloaded on 1/19/2026 11:19:46 AM. This article is licensed under a Creative Commons Attribution-NonCommercial 3.0 Unported Licence.

Open Access Article. Published on 06 January 2025. Downloaded on 1/19/2026 11:19:46 AM.
This article is licensed under a Creative Commons Attribution-NonCommercial 3.0 Unported Licence.

based materials have low specific capacities and limited potential for further optimization. Therefore, the development of an effective strategy to transform ZIFs into composites of metal oxides and CNTs as mentioned above is highly attractive but challenging.

Here, we develop an efficient synthesis strategy that involves reductive pyrolysis followed by oxidative pyrolysis of Zn/Co-ZIF to produce ZnO and Co_3O_4 double oxides encapsulated in carbon nanotubes (denoted as ZnO/Co_3O_4@CNTs) as anode materials for high-performance LIBs. This newly designed electrode material consists of Co_3O_4 and ZnO nanoparticles that are uniformly encapsulated in interconnected CNTs, combining the structural advantages of various functional components. The double TMO (ZnO and Co_3O_4) nanoparticles expose numerous active sites for lithium insertion undergoing conversion and alloying reactions which can enhance the redox reaction kinetics. Meanwhile, the high strength and flexibility of CNT coatings increase conductivity, prevent particle aggregation, and significantly improve material stability. These multifunctional components contribute to superior rate performance and excellent cyclability of ZnO/Co_3O_4@CNTs in LIBs applications, achieving a high specific capacity of 1156 mA h g^{-1} after undergoing 200 cycles at the operating current density of 200 mA g^{-1}.

2 Results and discussion

2.1 Synthesis and characterization of ZnO/Co_3O_4@CNTs

Fig. 1a illustrates the synthesis route of ZnO/Co_3O_4@CNTs. Initially, the Zn/Co-ZIF precursor was synthesized using water and *n*-butylamine as the solvent and regulator, respectively. The scanning electron microscopy (SEM) and transmission electron microscopy (TEM) images of Zn/Co-ZIF reveal the uniformly distributed dodecahedral particles with an average diameter of about 800 nm (Fig. S1a and b†). The powder X-ray diffraction (XRD) patterns confirm the phase purity of Zn/Co-ZIF (Fig. S1c†).

Zn/Co-ZIF was then pyrolyzed at 400 °C for 2 hours, followed by 800 °C for 1.5 hours in a hydrogen–argon mixture to form Zn and Co wrapped by carbon (Zn/Co@CNTs). The XRD patterns of Zn/Co@CNTs reveal peaks at 45° and 51°, corresponding to metal Co (Fig. S2c†). Zn/Co@CNTs retains the dodecahedron shape, though with a slightly reduced size due to shrinkage during pyrolysis. The surface of the metal nanoparticles is wrapped by CNTs, forming a three-dimensional conductive network that prevents nanoparticle aggregation (Fig. S2a and b†). The material pyrolyzed only at 400 or 800 °C shows no formation of CNTs (Fig. S3†), demonstrating the critical role of the dual-step pyrolysis in producing the CNT structure. Therefore, the first-step pyrolysis at 400 °C is critical to generate Co

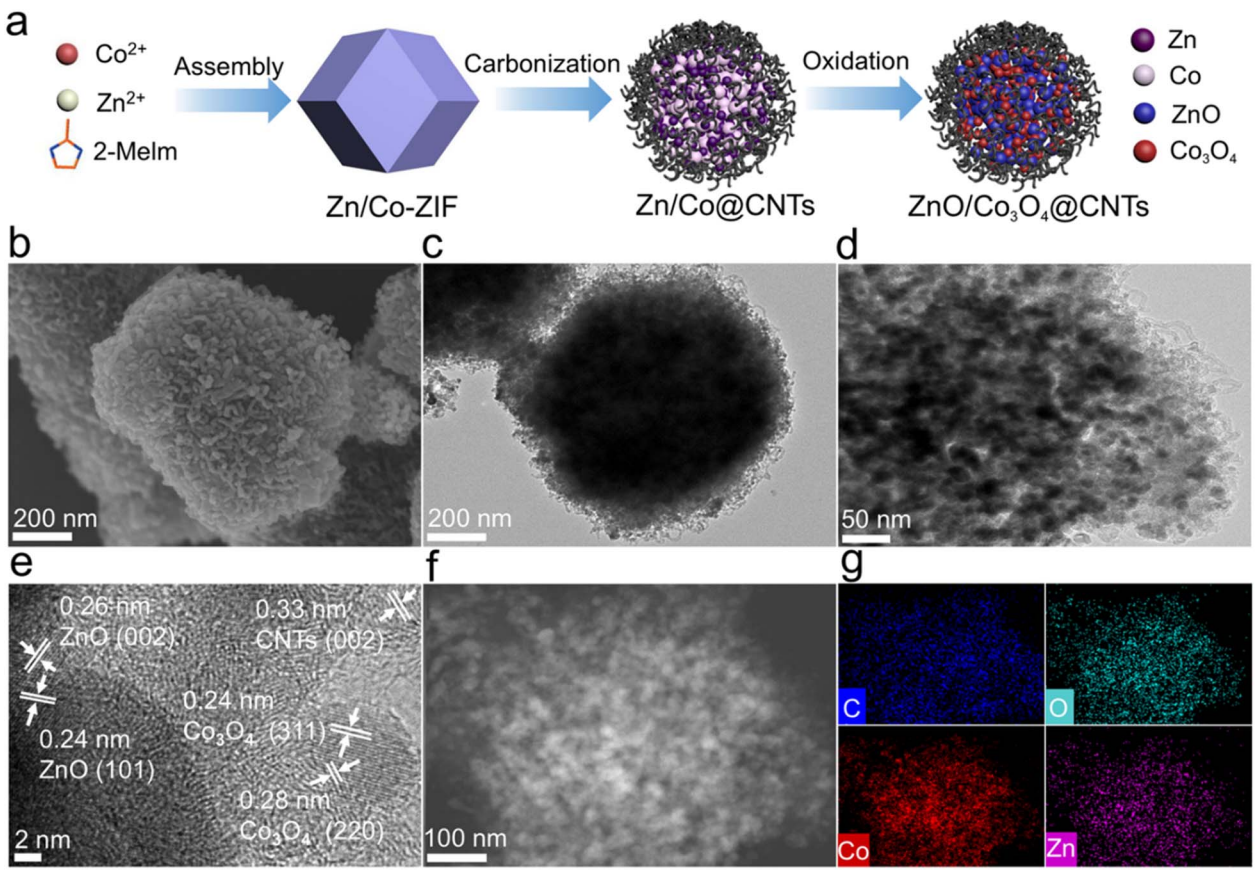

Fig. 1 (a) The synthesis route of ZnO/Co_3O_4@CNTs. (b) SEM, (c and d) TEM, (e) HRTEM images of ZnO/Co_3O_4@CNTs, (f) HAADF image of ZnO/Co_3O_4@CNTs and (g) the corresponding elemental mapping of C, O, Co, and Zn.

© 2025 The Author(s). Published by the Royal Society of Chemistry

Open Access Article. Published on 06 January 2025. Downloaded on 1/19/2026 11:19:46 AM.
This article is licensed under a Creative Commons Attribution-NonCommercial 3.0 Unported Licence.

nanoparticles,[25,26] which act as catalysts for the formation of CNTs at 800 °C.[27]

Finally, Zn/Co@CNTs was oxidized at 400 °C to obtain ZnO/Co_3O_4@CNTs (Fig. 1b and c). SEM images show loose CNTs on the surface after oxidation treatment. TEM image displays nanoparticles with a size of about 10 nm confined within CNTs (Fig. 1d). The high-resolution TEM image shows clear lattice fringes of 0.26, 0.24, and 0.33 nm, corresponding to the (002) plane of ZnO, (311) plane of Co_3O_4, and (002) plane of CNTs, respectively (Fig. 1e).[28] Elemental analysis indicates that O, Co, and Zn elements are distributed inside, and C, N elements are uniformly scattered on the surface (Fig. 1f, g and S4†). XRD patterns of ZnO/Co_3O_4@CNTs reveal typical diffraction peaks for ZnO and Co_3O_4 (Fig. 2a), which are in accordance with the TEM observation. Additionally, no diffraction peak is observed pertaining to CNTs, due to the much stronger crystalline peak intensity of metal oxides.

Oxidation duration studies show sharper XRD diffraction peaks of oxide at longer oxidation times (Fig. S5a†), implying increased crystallinity and particle size of oxides. Raman spectroscopy reveals characteristic D (1347 cm^{-1}) and G bands (1574 cm^{-1}) of carbon, with increased D/G intensity ratio with oxidation time, suggesting reduced graphitization (Fig. S5b†).[29] The effect of oxidation time on the composition of the composites was monitored by energy-dispersive X-ray spectroscopy (Fig. S6†). With the increase of oxidation time, the carbon contents are decreased while the O contents are increased. These results demonstrate that the increase in oxidation time results in the increased content of metal oxides and decreased content of CNTs. An optimal oxidation time of 10 minutes was determined based on comprehensive analysis, balancing CNT formation and structural integrity (Fig. S7†).

Moreover, the chemical state and elemental composition of ZnO/Co_3O_4@CNTs were further investigated by X-ray photoelectron spectroscopy (XPS) (Fig. 2d–i). The survey spectra confirm the presence of C, N, O, Co, and Zn. The existence of C is evidenced specifically through the identification of distinct peaks at energy levels of 284.6, 285.3, 286.4, and 289 eV, which are attributed to the C=O, C–O, C=N, and C–C bonds (Fig. 2e).[27] The fitting curve of N 1s displays three peaks at 398.5, 399.3, and 400.2 eV, corresponding to pyridinic, pyrrolic, and graphite N, respectively (Fig. 2f).[30] The O 1s spectrum is deconvoluted into three different peaks at 531.6, 532.9, and 529.5 eV, implying the existence of C–O, C=O, and Co/Zn–O in ZnO and Co_3O_4 (Fig. 2g). The Zn 2p spectrum shows two peaks at 1044.7 and 1021.7 eV (Fig. 2h), confirming the presence of

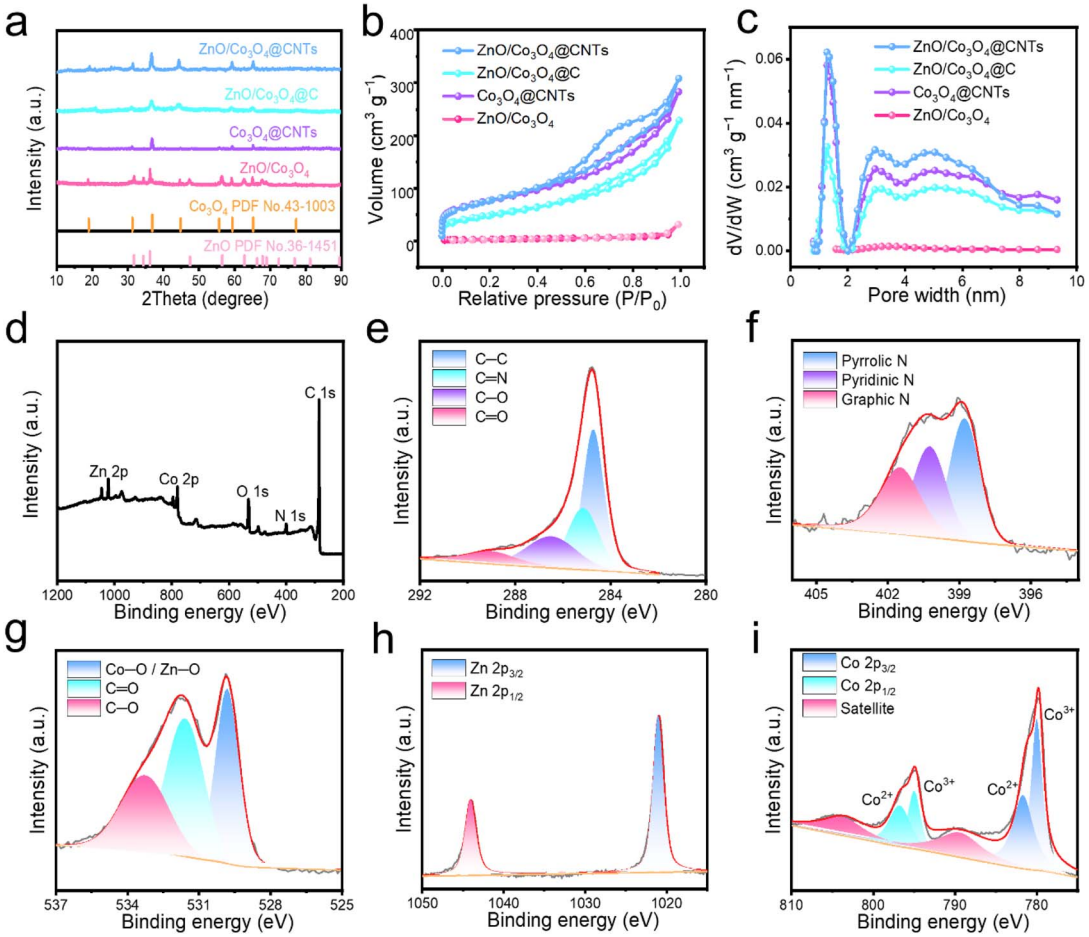

Fig. 2 (a) XRD patterns, (b) nitrogen adsorption–desorption isotherms, and (c) pore size distributions of the samples. (d) XPS survey spectrum of ZnO/Co_3O_4@CNTs. (e) High-resolution C 1s, (f) N 1s, (g) O 1s, (h) Zn 2p, and (i) Co 2p XPS spectra of the ZnO/Co_3O_4@CNTs.

Open Access Article. Published on 06 January 2025. Downloaded on 1/19/2026 11:19:46 AM.
This article is licensed under a Creative Commons Attribution-NonCommercial 3.0 Unported Licence.

Zn^{2+} in ZnO. The peaks at 780.6 and 795.9 eV in the high-resolution Co 2p spectrum correspond to Co $2p_{3/2}$ and Co $2p_{1/2}$ levels of Co^{2+}, while the peaks at 779.5 eV and 794.4 eV are assigned to Co^{3+} (Fig. 2i).[31–33]

For comparison, ZnO and Co_3O_4 wrapped by carbon (denoted as ZnO/Co_3O_4@C) and ZnO/Co_3O_4 were synthesized using Zn/Co-ZIF as the precursor. The SEM and TEM images show agglomerated particles for ZnO/Co_3O_4, highlighting the importance of CNTs in preventing metal aggregation (Fig. S8 and S9†). Single Co_3O_4 wrapped by carbon nanotubes (denoted as Co_3O_4@CNTs) derived from ZIF-67 was also prepared (Fig. S10†). Raman spectra show that Co_3O_4@CNTs has the lowest $I_D : I_G$, indicating the formation of highly graphitized CNTs due to the high content of Co (Fig. S11†).

The nitrogen adsorption/desorption isotherms show that ZnO/Co_3O_4@CNTs possesses a higher specific surface area (306.3 $m^2\ g^{-1}$) than ZnO/Co_3O_4@C (279.4 $m^2\ g^{-1}$), Co_3O_4@CNTs (180.3 $m^2\ g^{-1}$), and ZnO/Co_3O_4 (9.6 $m^2\ g^{-1}$) (Fig. 2b). The high surface area of ZnO/Co_3O_4@CNTs is beneficial for Li^+ storage. The pore size distribution curve indicates that ZnO/Co_3O_4@CNTs has abundant micropores and mesopores (Fig. 2c), which can facilitate fast Li^+ transports and enhance electrochemical kinetics. The contents of Zn and Co are measured to be 4.2 and 32.1 wt% by atom absorption spectroscopy (AAS), respectively (Table S1†). Therefore, the contents of ZnO, Co_3O_4, and CNTs are calculated to be 5.2, 43.7, and 51.1 wt%, respectively. The content of CNTs in the ZnO/Co_3O_4@CNTs was further measured by thermogravimetric analysis (TGA) under a flow air atmosphere. The TGA curve shows two weight-loss stages (Fig. S12†). The first stage is the evaporation of the adsorbed water, with a weight loss of about 4.32 wt%. The second stage shows a weight loss of 52.5 wt%, corresponding to the combustion of carbon after 350 °C. Therefore, the content of CNTs is 52.5 wt%, which is consistent with the AAS results. These comprehensive characterizations demonstrate the successful synthesis and potential application of ZnO/Co_3O_4@CNTs in LIBs.

2.2 Electrochemical performance of ZnO/Co_3O_4@CNTs for LIBs

To assess the electrochemical performance of the materials as anodes in LIBs, cyclic voltammetry (CV) tests were conducted at

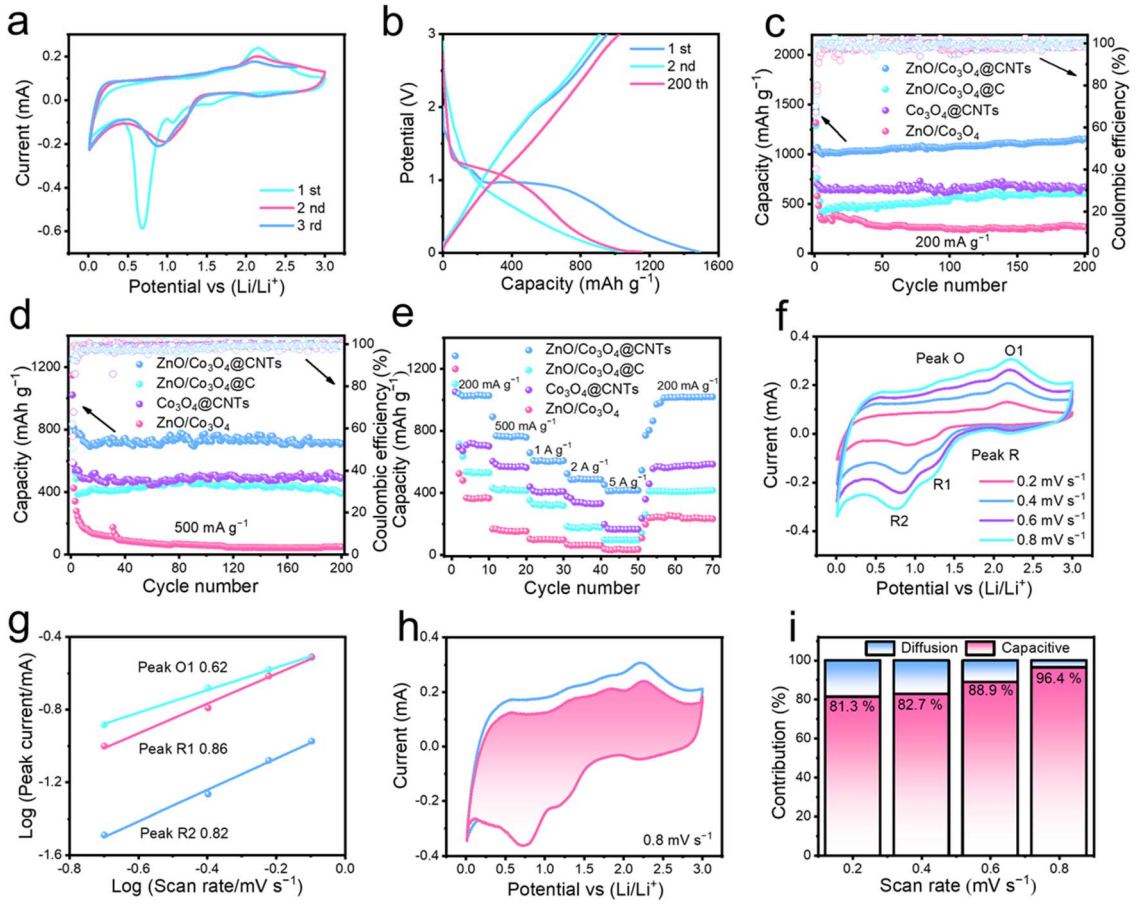

Fig. 3 (a) The CV curves of ZnO/Co_3O_4@CNTs in the first, second, and third cycles at the scan rate of 0.2 mV s^{-1} and (b) the galvanostatic discharge/charge curves of ZnO/Co_3O_4@CNTs at a current density of 200 mA g^{-1}. (c and d) The cycling performance and (e) the rate performance of the samples. (f) CV curves of ZnO/Co_3O_4@CNTs at different scan rates from 0.2 to 0.8 mV s^{-1}, (g) the *b*-values calculated by plotting the peak current *versus* the scan rate, (h) the separated regions of capacitive and diffusion-controlled behavior at 0.8 mV s^{-1}, and (i) the contribution ratio of capacitive capacity at different scan rates of ZnO/Co_3O_4@CNTs.

© 2025 The Author(s). Published by the Royal Society of Chemistry

Open Access Article. Published on 06 January 2025. Downloaded on 1/19/2026 11:19:46 AM. This article is licensed under a Creative Commons Attribution-NonCommercial 3.0 Unported Licence.

the scan rate of 0.2 mV s^{-1} (Fig. 3a and S13†). During the initial reduction, a peak at 0.45 V corresponds to the reduction of ZnO to Zn and the formation of amorphous Li_2O. The peak at 0.07 V indicates the alloying of Zn with Li^+ to form various lithium zinc alloys (LiZn, Li_2Zn_3, $LiZn_2$, Li_2Zn_5). Peaks at 0.7 and 0.8 V are attributed to the reduction of Co^{2+} to Co and Co^{3+} to Co^{2+}, respectively. During the oxidation process, a peak at 2.1 V corresponds to the oxidation of Co to Co_3O_4. Peaks at 0.7 V and 0.4 V indicate the dealloying of the lithium zinc alloys, while a peak at approximately 1.5 V marks the reversible redox conversion between Zn and Li_2O to form ZnO. The electrochemical reactions occurring in the half-cell system are illustrated in the ESI.† The nearly identical peak intensities and integral areas in the CV curves of the 2nd and 3rd cycles reveal the good reversibility of Li^+ insertion and extraction reactions.

Typical charge–discharge curves at a current density of 200 mA g^{-1} are shown in Fig. 3b and S14a–c.† ZnO/Co_3O_4@CNTs exhibits the initial discharge and charge capacities of 1460 and 1026 mA h g^{-1}, respectively, corresponding to an initial Coulomb efficiency (ICE) of 70.3%. The irreversible capacity reduction is attributed to electrolyte decomposition and solid electrolyte interphase (SEI) formation.[34] The presence of SEI membrane is crucial for the performance of the battery when it acts as a protective layer, preventing further degradation of the electrolyte and ensuring the stability of the battery. After the initial rapid capacity loss, the reversible capacity remains stable, and the coulombic efficiency (CE) approaches 100%. The nearly overlapped discharge–charge capacities indicate the good reversibility and stability of the ZnO/Co_3O_4@CNTs electrode.

Electrochemical cycling performance was evaluated at a constant current density of 200 mA g^{-1} (Fig. 3c). The ZnO/Co_3O_4@CNTs electrode maintains a high specific capacity of 1156 mA h g^{-1} after 200 cycles, with a minimal capacity loss rate of about 0.54‰ for each cycle. Even at a higher current density of 500 mA g^{-1}, the ZnO/Co_3O_4@CNTs electrode still demonstrates an impressive capacity of 710 mA h g^{-1} with a capacity holding ratio of 61.7% (Fig. 3d). The measured specific capacities exceed the theoretical one (621.1 mA h g^{-1}), which can be attributed to the pseudocapacitive behavior caused by the porous carbon nanotubes in facilitating the storage of Li^+. In comparison, ZnO/Co_3O_4 shows an initial specific capacity of 1148.5 mA h g^{-1} but drops significantly to 50.7 mA h g^{-1} after 200 cycles with a capacity holding ratio of only 4.4%. The similar initial specific capacity of ZnO/Co_3O_4 indicates that the active ZnO and Co_3O_4 contribute to the main capacity. Nevertheless, the ZnO/Co_3O_4 electrode generates remarkable capacity attenuation, which may be due to the absence of CNTs to buffer volume expansion, resulting in reduced active material utilization rate and irreversible capacity consumption. ZnO/Co_3O_4@C maintains a specific capacity of 391.4 mA h g^{-1} after 200 cycles with 38.3% retention of the initial one, unequivocally showing how crucial the highly graphitized CNT protective layers are in improving the stability and conductivity of metal oxide-based materials used in LIBs. Co_3O_4@CNTs maintains a specific capacity of 536.8 mA h g^{-1} after 200 cycles with a capacity retention rate of 52.6%. The exhibited lower specific capacity of Co_3O_4@CNTs compared to ZnO/Co_3O_4@CNTs implies that the ZnO performs both conversion and alloying reactions facilitating the reversible lithium deintercalation/intercalation, which improved lithium storage performance.

The ability to withstand various current densities was evaluated. ZnO/Co_3O_4@CNTs delivers reversible specific capacities of 1283.8, 718.2, 608, 486.3, and 417.5 mA h g^{-1} at current densities of 0.2, 0.5, 1, 2, and 5 A g^{-1}, respectively. When the current density returns from 5 to 0.2 A g^{-1}, the capacity restores to 1018.6 mA h g^{-1}. In comparison, ZnO/Co_3O_4@C is only restored to 416.5 mA h g^{-1} (Fig. 3e), suggesting that the outstanding capacity retention of ZnO/Co_3O_4@CNTs is attributed to the three-dimensional interconnected CNTs with excellent stability. The superior electrochemical properties of ZnO/Co_3O_4@CNTs compared to other anode composites (Fig. S15 and Table S2†) demonstrate its potential for high-performance energy storage devices.

To investigate the changes in the ZnO/Co_3O_4@CNTs electrode after 200 cycles at 200 mA g^{-1}, SEM and TEM observations were conducted (Fig. S16a–c†). The morphology of the composite is mostly preserved after the repeated lithiation/delithiation process, indicating the critical role of the protective CNT layer in preserving the structural integrity of the material. Additionally, XRD measurements were performed to assess the crystal composition of the electrode materials after prolonged charge–discharge cycles (Fig. S16d†). The XRD results are consistent with the phase of ZnO/Co_3O_4@CNTs before cycling, confirming the effective reversibility of the redox reactions during the lithiation and delithiation processes. These findings significantly contribute to the excellent electrochemical performance of the ZnO/Co_3O_4@CNTs electrode.

To explore the lithium storage mechanism, multi-scan rate CV tests were conducted at scan rates ranging from 0.2 to 0.8 mV s^{-1} (Fig. 3f and S17–19†). Charge storage mechanisms include capacitive behavior (surface storage processes) and diffusion-controlled behavior (reactions within the active material). The b values were calculated to determine the dominant mechanism, with values of 0.5 indicating diffusive behavior, 1 indicating capacitive behavior, and values between 0.5 and 1 indicating a hybrid mechanism.[35] The calculated b value for ZnO/Co_3O_4@CNTs is 0.62 for the anodic process and 0.86 and 0.82 for the cathodic process (Fig. 3g), suggesting a predominant hybrid mechanism.[36,37] The pseudocapacitance contributions were calculated at various scan rates, which were 81.3, 82.7, 88.9, and 96.4% at 0.2, 0.4, 0.6, and 0.8 mV s^{-1}, respectively (Fig. 3h, i and S20†). The pseudocapacitance contribution of ZnO/Co_3O_4@CNTs surpasses that of ZnO/Co_3O_4@C, Co_3O_4@CNTs, and ZnO/Co_3O_4 (Fig. S21–S23†), which is conducive to the superior rate capability of ZnO/Co_3O_4@CNTs.

Electrochemical impedance spectroscopy (EIS) was employed to measure the charge transfer resistance (R_{ct}) and Li^+ diffusion impedance (Z_w) based on the semicircles on the high-frequency band and the diagonal lines on the low frequency in the Nyquist plots of the cells.[38,39] The respective equivalent circuit is shown in the inset of Fig. 4a. ZnO/Co_3O_4@CNTs has a lower R_{ct} than ZnO/Co_3O_4@C and ZnO/Co_3O_4 (Fig. 4a and

Open Access Article. Published on 06 January 2025. Downloaded on 1/19/2026 11:19:46 AM. This article is licensed under a Creative Commons Attribution-NonCommercial 3.0 Unported Licence.

Table S3†), benefiting from the outer CNTs which provide efficient electronic transmission channels to facilitate charge transfer. In the low-frequency region, the slope of ZnO/Co_3O_4@CNTs is the maximum and the Z_w value is the lowest, suggesting that the low Li^+ insertion potential of CNTs wrapped in the outer layer and the bimetallic oxides as abundant active sites performing rich conversion and alloying reactions enhance the Li^+ insertion and diffusion.

In situ EIS measurements during the first discharge cycle at 200 mA g^{-1} recorded the changes in SEI resistance (R_{SEI}) of the ZnO/Co_3O_4@CNTs electrode. The EIS spectra at different voltages are shown in Fig. 4b. Initially, R_{SEI} drops dramatically and remains stable within a specific capacity range of 300 to 1300 mA h g^{-1} (Fig. 4c), validating the quick formation and stability of the SEI. According to the Nyquist plot of the ZnO/Co_3O_4@CNTs composite material after different charge–discharge cycles (Fig. 4d), the unlithiated original material exhibits greater impedance due to the lower permeability of the electrolyte in the active material. A notable reduction in impedance was observed after the completion of the first cycle of charging and discharging. As activation progresses, the porous structure and conductive CNTs ensure ample interaction between the electrolyte and the active material, and make the impedance diminish gradually and remain remarkably stable after the 50th cycle, demonstrating that ZnO/Co_3O_4@CNTs possesses excellent interfacial contact and structural stability.

The galvanostatic intermittent titration technique (GITT) was utilized to analyze the Li^+ diffusion behavior.[36,40] The average Li^+ diffusion coefficiency (D_{Li^+}) for ZnO/Co_3O_4@CNTs is 1.1×10^{-9} cm^2 s^{-1}, almost an order of magnitude larger than that of the ZnO/Co_3O_4@C electrode (4.21×10^{-10} cm^2 s^{-1}), Co_3O_4@CNTs electrode (5.58×10^{-10} cm^2 s^{-1}), and ZnO/Co_3O_4 electrode (3.23×10^{-10} cm^2 s^{-1}) during both Li^+ embedding and de-embedding processes (Fig. 4e, f, S24, and Table S4†). This result indicates that CNTs with exceptional conductivity and ZnO and Co_3O_4 with plentiful active sites jointly accelerate the ion motion and optimize ion diffusion kinetics to reach charge equilibrium and inhibit net charge accumulation. To explore the underlying reasons for carbon material properties on the Li^+ transport capacity, Kelvin probe force microscopy (KPFM) was carried out to test the work functions of ZnO/

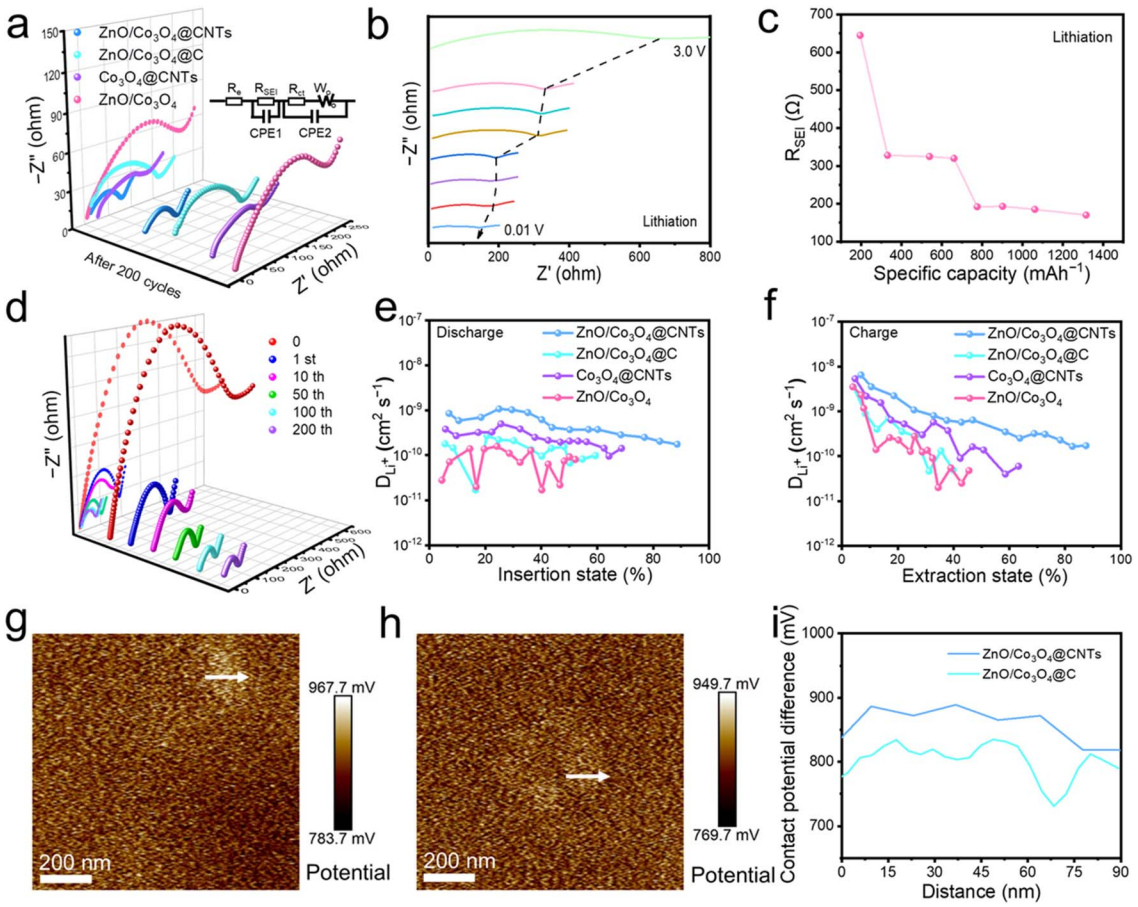

Fig. 4 (a) Nyquist plots after cycles of ZnO/Co_3O_4@CNTs, ZnO/Co_3O_4@C, Co_3O_4@CNTs, and ZnO/Co_3O_4 (inset is the equivalent circuit model). (b) The EIS profiles during the first discharge process and (c) corresponding fitting results of the R_{SEI} and specific capacity of ZnO/Co_3O_4@CNTs. (d) Nyquist plots after different numbers of cycles of ZnO/Co_3O_4@CNTs. (e) Li^+ diffusion coefficients in the discharge and (f) charge process of samples. Contact potential difference diagram of (g) ZnO/Co_3O_4@CNTs and (h) ZnO/Co_3O_4@C. (i) The line scanning contact potential difference of ZnO/Co_3O_4@CNTs and ZnO/Co_3O_4@C.

© 2025 The Author(s). Published by the Royal Society of Chemistry

Open Access Article. Published on 06 January 2025. Downloaded on 1/19/2026 11:19:46 AM.
This article is licensed under a Creative Commons Attribution-NonCommercial 3.0 Unported Licence.

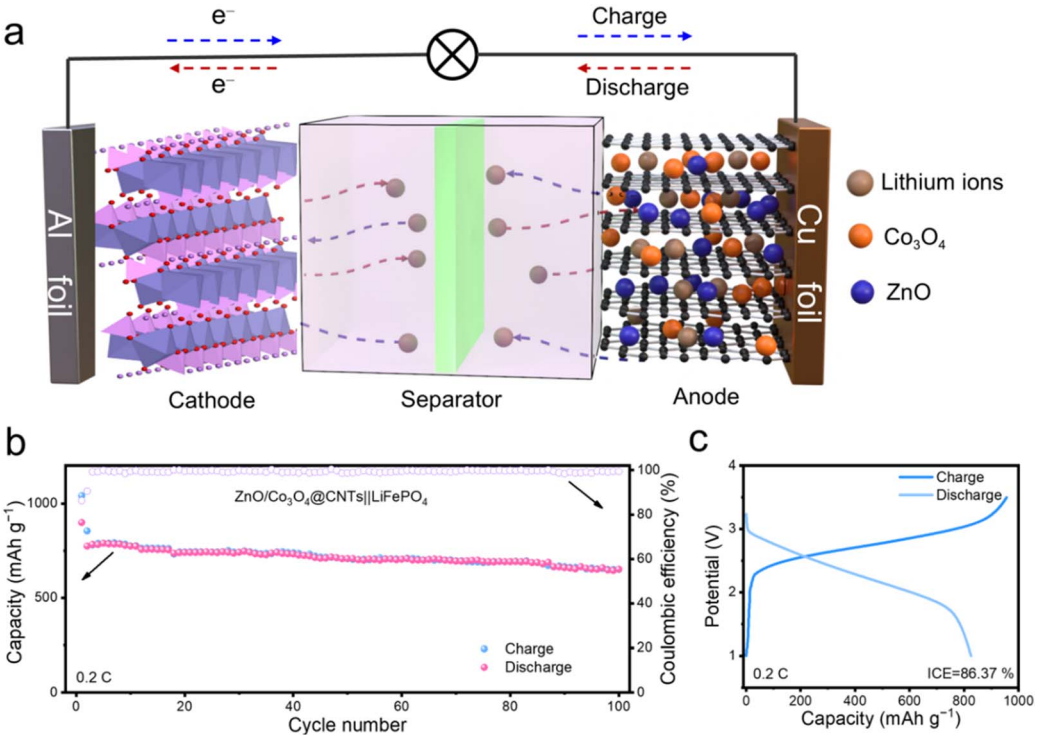

Fig. 5 (a) Schematic illustration of the full cell of ZnO/Co_3O_4@CNTs||LFP. (b) Cycling performance and (c) discharge and charge profiles of the full cell at the current density of 0.2 C.

Co_3O_4@CNTs and ZnO/Co_3O_4@C. The lower work function value indicates easier charge escape from the surface. The work functions (Fig. 4g–i, and Tables S5 and 6†) of ZnO/Co_3O_4@CNTs and ZnO/Co_3O_4@C are calculated to be 4.083 and 4.146 eV, respectively, implying that CNTs can facilitate ion transport and significantly improve multiplicity performance.

The practical application of ZnO/Co_3O_4@CNTs was evaluated by assembling full batteries with commercial lithium iron phosphate (LFP) cathodes and pre-lithiated anodes (Fig. 5a). Charge–discharge tests were conducted at a constant current density of 0.2 C over a voltage range of 1.0–3.5 V, yielding an ICE of approximately 86.36% (Fig. 5c). After 100 cycles, the ZnO/Co_3O_4@CNTs||LFP battery retained a discharge capacity of 652.1 mA h g^{-1} and 0.52 mA h cm^{-2}(Fig. 5b and S25†), demonstrating the outstanding electrochemical performance of ZnO/Co_3O_4@CNTs. The combination of the ZnO/Co_3O_4@CNTs electrode and LFP cathode shows promising potential for developing high-performance LIBs.

3 Conclusion

In conclusion, we have successfully developed a novel porous ZnO/Co_3O_4@CNTs nanocomposite *via* a pyrolysis-oxidation strategy, which can be utilized as a multifunctional anode material for LIBs. The hierarchically structured composite features internal double TMOs and external CNT conductive layers. This design optimizes Li^+ insertion from the electrolyte into the nanocomposite by leveraging the cooperative effects of multiple active sites. The ZnO and Co_3O_4 nanoparticles with abundant redox sites facilitate highly reversible Li^+ accommodation through multistep electrochemical reactions, thereby accelerating redox kinetics. Furthermore, the highly flexible CNT conductive layers significantly improve electron transfer, and act as robust physical barriers and chemical immobilization layers that buffer volume expansion and improve material stability. The combined functionalities of the nanocomposite endow ZnO/Co_3O_4@CNTs with excellent electrochemical performance in LIBs, exhibiting a high reversible specific capacity of 1156 mA h g^{-1} at 200 mA g^{-1} after running for 200 cycles. This work presents a new strategy for synthesizing ZIF-derived nanocomposites, showing great potential for application in high-performance LIBs.

Data availability

The data supporting this article have been included as part of the ESI.†

Author contributions

L. C. and Y. L. supervised the project. S. Q. performed material synthesis, characterization, and catalytic tests. J. W. helped with data analysis. S. Q., L. C., and Y. L. wrote the manuscript. All authors discussed the research.

Conflicts of interest

The authors declare no competing interests.

Open Access Article. Published on 06 January 2025. Downloaded on 1/19/2026 11:19:46 AM. This article is licensed under a Creative Commons Attribution-NonCommercial 3.0 Unported Licence.

Acknowledgements

This work was supported by the National Natural Science Foundation of China (No. 22138003, 22108083, 22378136, 22422806, and 21825802), the Guangdong Pearl River Talents Program (No. 2021QN02C847 and 2021ZT09Z109), the Natural Science Foundation of Guangdong Province (No. 2023B1515040005, 2023A1515010312, and 2024A1515011196), the Guangzhou Municipal Science and Technology Project (2025A04J5244), the Fundamental Research Funds for the Central Universities (2024ZYGXZR011), and the State Key Laboratory of Pulp and Paper Engineering (No. 2022C04, 2022ZD05, 2023PY06, and 2024ZD09).

References

1 J. Li, Y. Cai, H. Wu, Z. Yu, X. Yan, Q. Zhang, T. Z. Gao, K. Liu, X. Jia and Z. Bao, *Adv. Energy Mater.*, 2021, **11**, 2003239.
2 A. Manthiram, *ACS Cent. Sci.*, 2017, **3**, 1063–1069.
3 M. Zheng, H. Tang, Q. Hu, S. Zheng, L. Li, J. Xu and H. Pang, *Adv. Funct. Mater.*, 2018, **28**, 1707500.
4 W. Min, X. Chen, S. Huang, Y. Liao, Z. Liang, Y. Lei and J. Xu, *Carbon*, 2023, **210**, 118038.
5 M. Agostini, S. Brutti and J. Hassoun, *ACS Appl. Mater. Interfaces*, 2016, **8**, 10850–10857.
6 M. Akhilash, P. S. Salini, B. John and T. D. Mercy, *J. Alloys Compd.*, 2021, **869**, 159239.
7 J. Zhang and A. Yu, *Sci. Bull.*, 2016, **60**, 823–838.
8 M. Zheng, H. Tang, L. Li, Q. Hu, L. Zhang, H. Xue and H. Pang, *Adv. Sci.*, 2018, **5**, 1700592.
9 M. Kundu, D. Xiong, R. Thomas and L. Liu, *J. Alloys Compd.*, 2021, **888**, 161626.
10 S. Shilpi, M. S. Anantha, H. B. Muralidhara and M. Kundu, *Mater. Lett.*, 2021, **308**, 131298.
11 Y. Chen, Y. Meng, C. Zhang, H. Yang, Y. Xue, A. Yuan, X. Shen and K. Xu, *J. Power Sources*, 2019, **421**, 41–49.
12 X. Yang, H. Wang, Y. Song, K. Liu, T. Huang, X. Wang, C. Zhang and J. Li, *ACS Appl. Mater. Interfaces*, 2022, **14**, 26873–26881.
13 J.-T. Lei, Y.-Q. Wang, Z.-A. Li, P.-P. Chen, J.-Z. Chen, Y.-L. Hou and D.-L. Zhao, *J. Alloys Compd.*, 2023, **969**, 172376.
14 D. Wang, H. He, L. Han, R. Lin, J. Wang, Z. Wu, H. Liu and H. L. Xin, *Nano Energy*, 2015, **20**, 212–220.
15 H. Ye, G. Zheng, X. Yang, D. Zhang, Y. Zhang, S. Yan, L. You, S. Hou and Z. Huang, *J. Electroanal. Chem.*, 2021, **898**, 115652.
16 C. Liao and S. Wu, *Chem. Eng. J.*, 2018, **355**, 805–814.
17 S. Wu, M. Lu, X. Tian and C. Jiang, *Chem. Eng. J.*, 2016, **313**, 610–618.
18 X. Tang, M. Liang, Y. Zhang, W. Sun and Y. Wang, *Dalton Trans.*, 2019, **48**, 4413.
19 X. Tan, Y. Wu, X. Lin, A. Zeb, X. Xu, Y. Luo and J. Liu, *Inorg. Chem. Front.*, 2020, **7**, 4939–4955.
20 G. Song, Y. Shi, S. Jiang and H. Pang, *Adv. Funct. Mater.*, 2023, **33**, 2303121.
21 L. Chen, H.-F. Wang, C. Li and Q. Xu, *Chem. Sci.*, 2020, **11**, 5369.
22 X. Peng, L. Chen and Y. Li, *Mol. Catal.*, 2022, **529**, 112568.
23 Z. Tai, M. Shi, S. Chong, Y. Chen, C. Shu, X. Dai, Q. Tan and Y. Liu, *J. Alloys Compd.*, 2019, **800**, 1–7.
24 J. Ding, H.-F. Wang, X. Yang, W. Ju, K. Shen, L. Chen and Y. Li, *Natl. Sci. Rev.*, 2022, **10**, nwac231.
25 G. Chen, L. Wang, Y. Liu, M. Xin, Z. Cao and Y. Zhang, *New J. Chem.*, 2023, **47**, 14169–14176.
26 C. Young, J. Kim, Y. V. Kaneti and Y. Yamauchi, *ACS Appl. Energy Mater.*, 2018, **1**, 2007–2015.
27 W. Zhang, X. Jiang, X. Wang, Y. V. Kaneti, Y. Chen, J. Liu, J.-S. Jiang, Y. Yamauchi and M. Hu, *Angew. Chem., Int. Ed.*, 2017, **129**, 8555–8560.
28 J. Zhao, S. Yao, C. Hu, Z. Li, J. Wang and X. Feng, *Mater. Lett.*, 2019, **250**, 75–78.
29 C. Hu, Y. Zhang, A. Hu, Y. Wang, X. Wei, K. Shen, L. Chen and Y. Li, *Adv. Mater.*, 2023, **60**, 23729.
30 L. Wang, Z. Wang, L. Xie, L. Zhu and X. Cao, *ACS Appl. Mater. Interfaces*, 2019, **11**, 16619–16628.
31 J. Liu, G. Li, D. Luo, J. Li, X. Zhang, Q. Li, H. Li, Y. Zhang and Z. Chen, *Adv. Funct. Mater.*, 2023, **34**, 2303357.
32 W. Yao, A. Hu, J. Ding, N. Wang, Z. Qin, X. Yang, K. Shen, L. Chen and Y. Li, *Adv. Mater.*, 2023, **35**, 2301894.
33 W. Yao, J. Chen, Y. Wang, R. Fang, Z. Qin, X. Yang, L. Chen and Y. Li, *Angew. Chem., Int. Ed.*, 2021, **60**, 23729.
34 H. You, X. Wang, J. Zhu, B. Jiang, G. Han, X. Wei and H. Dai, *Energy Storage Mater.*, 2023, **65**, 103083.
35 S. Sengupta and M. kundu, *Energy Technol.*, 2022, **10**, 2200117.
36 P. Wang, S. Sun, Y. Jiang, Q. Cai, Y.-H. Zhang, L. Zhou, S. Fang, J. Liu and Y. Yu, *ACS Nano*, 2020, **14**, 15577–15586.
37 W. Li, D. Wang, Z. Gong, Z. Yin, X. Guo, J. Liu, C. Mao, Z. Zhang and G. Li, *ACS Nano*, 2020, **14**, 16046–16056.
38 H. J. Kwon, J.-Y. Hwang, H.-J. Shin, M.-G. Jeong, K. Y. Chung, Y.-K. Sun and H.-G. Jung, *Nano Lett.*, 2020, **20**, 625–635.
39 Q. Pan, Y. Wu, F. Zheng, X. Ou, C. Yang, X. Xiong and M. Liu, *Chem. Eng. J.*, 2018, **348**, 653–660.
40 B. Sun, Q. Zhang, C. Zhang, W. Xu, J. Wang, G. Yuan, W. Lv, X. Li and N. Yang, *Adv. Energy Mater.*, 2021, **11**, 2100082.

© 2025 The Author(s). Published by the Royal Society of Chemistry